The effects of varying the annealing period on the structure, morphology and optical properties of $MgAl_2O_4$:0.1% Mn^{2+} nanophosphors

C. Dlamini[1,*], M. R. Mhlongo[1], L. F. Koao[2], T. E. Motaung[3], T. T. Hlatshwayo[4], S. V. Motloung[1,5,*]

[1]Department of Physics, Sefako Makgatho Health Science University, P. O. Box 94, Medunsa, 0204, South Africa

[2]Department of Physics, University of the Free State (Qwaqwa Campus), Private Bag X 13, Phuthaditjhaba, 9866, South Africa

[3]Department of Chemistry, University of Zululand, Kwadlangezwa, 3886, South Africa

[4]Department of Physics, University of Pretoria, Pretoria, 0002, South Africa

[5]Department of Physics, Nelson Mandela University (NMU), P. O. Box 77000, Port Elizabeth, 6031, South Africa

*Correspondence to C. Dlamini (dlaminiclinton@gmail.com) or S. V. Motloung (cchataa@gmail.com).

Abstract

In this study, magnesium aluminate nanopowders doped with manganese ions ($MgAl_2O_4$:0.1% Mn^{2+}) were prepared by citrate sol–gel technique. The consequences on the structural, morphological and optical properties when varying the annealing period (AP) at a fixed annealing temperature of 800 °C and dopant concentration (0.1% Mn^{2+}) were investigated. The AP was varied at the range of 1–6 h. X-ray powder diffraction (XRD) results showed that doping with 0.1% Mn^{2+} and varying the AP did not influence the crystal structure of the host (un-doped) material. The scanning electron microscope (SEM) images suggested that doping does not influence the morphology of the prepared nanopowders and varying the AP slightly influence the particle size. Transition electron microscopy (TEM) image suggested that the crystallite sizes were below 15 nm. The ultraviolet–visible (UV–Vis) diffuse reflection spectroscopy showed that the band gap of the $MgAl_2O_4$:0.1% Mn^{2+} can be tuned from 5.04 to 4.58 eV with varying AP. Photoluminescence (PL) results showed two emission peaks located at around 413 and 655 nm. They were attributed to the defect levels within the host material and to the ($^4T_1 \rightarrow {}^6A_1$) transitions of Mn^{2+}, respectively. Increasing the AP significantly influences the luminescence of the prepared powders. The CIE coordinate results showed that the bluish emission colour can be changed to the violet region when AP was increased.

Keywords: Citrate sol–gel; $MgAl_2O_4$; Mn^{2+}; Luminescence; CIE

1 Introduction

Nanomaterial based on aluminates and other related oxides has been investigated and widely used as fluorescent lamp and plasma display panel phosphors [1]. They have been widely used because of their fascinating properties [2, 3]. Magnesium aluminate ($MgAl_2O_4$) is amongst the material that possesses these properties and has been considered in a variety of technological applications such as ceramics, transparent windows, lenses, humidity sensors, photocatalyst materials and catalyst support [4, 5]. $MgAl_2O_4$ nanopowders can be fabricated using different techniques such as combustion [6], co-precipitate [7], citrate sol–gel [8], solid state reaction [9] and freeze drying [10]. The sol–gel method was used in this study over other synthesis techniques due its low energy consumption, cheap, high quality control of particle size and constant morphology of the particles [10]. $MgAl_2O_4$ nanopowders can be easily doped by foreign atoms such as transition metals (TMs). Mn^{2+} is amongst the TM that has been intensively studied by many researchers because it shows an emission in the visible region and can be excited in many different ways [11]. The luminescent emission shows the radiative de-excitation from $^4T_1$ excited level to $^6A_1$ ground state energy level. Li et al. [12] reported the microstructure and luminescence properties of $MgAl_2O_4$:*x*% Mn^{2+} red-emitting phosphor. The PL results showed that Mn^{2+} exhibits a red emission band centred at 650 nm, which was assigned to the $^4T_1 \rightarrow {}^6A_1$ transition of Mn^{2+}. The optimal Mn doping content for the best luminescence was found to be 0.10%, which eventually serves as the main reason why 0.1% Mn^{2+} was kept constant in this study. Singh et al. [13] reported a study on luminescence investigation of the Mn^{2+} and Mn^{4+} doped calcium aluminate prepared via combustion method. PL results showed red emission from Mn^{2+} and Mn^{4+} ions. On the other hand, and apart from the Mn^{2+} doped studies, Melato et al. [14] reported the effects of annealing at different time intervals of $MgAl_2O_4$:0.3% In^{3+} nanophosphor prepared via citrate sol–gel. PL results showed two emission peaks at around 388 nm (violet) and 560 nm (green) both originated from the host material. The investigation on $MgAl_2O_4$:Mn^{2+} at AP of 8 h has already been reported in the literature [13] and Mn^{2+} is well known to emit red emission colour around 650 nm [12, 15]. However, the investigation on the effects of the AP on the $MgAl_2O_4$:0.1% Mn^{2+} have not been reported in the literature to date. This study investigates the effects of AP on the structure, morphology and optical properties of the $MgAl_2O_4$:0.1% Mn^{2+} phosphor material. The main aim of this study is to fabricate alternative oxide phosphor material for practical application such as in light emitting diode (LED). The observed excitations and emission channels are also discussed in detail.

2 Experimental

2.1 Synthesis

The un-doped and $MgAl_2O_4$:0.1% Mn^{2+} nanopowder samples were prepared using the citrate sol–gel method. The chemicals purchased from Sigma Aldrich were used to prepare the samples. The 3.808 g of $Mg(NO_3)_2 \cdot 6H_2O$ (98%), 10.919 g of $Al(NO_3)_3 \cdot 9H_2O$ (98%) and 2.328 g of citric acid (CA) $C_8H_8O_7 \cdot H_2O$ (99%) were dissolved in 30 ml of deionized water to prepare the un-doped $MgAl_2O_4$. The doped sample ($MgAl_2O_4$:0.1% Mn^{2+}) was prepared by adding 0.003 g of $Mn(NO_3)_3 \cdot 6H_2O$ (98%) to the solution. The solution stoichiometric molar ratio that was used for Mg:Al and Mg:CA was 1:2 and 1:0.075, respectively. The solution was heated at a temperature of ~ 80 °C using the magnetic stirrer until a gel was formed. The formed gels were dried up in an oven at 130 °C for 1 h and subsequently annealed in a furnace at 800 °C for various APs ranging from 1 to 6 h. The obtained solid like foam

product was ground to powderusing a mortar and pestle. The powdered samples were then taken for analysis using different techniques.

2.2 Characterization

Malvern panaltical aeris XRD with a Co-Ku (1.790 Å) was used to characterize the crystal structure. The surface morphology and elementary composition of the prepared phosphors were investigated using a Zeiss Supra 55 scanning electron microscope (SEM) with an energy dispersive X-ray spectroscopy (EDS). JEOL JEM 1010 transmission electron microscopy (TEM) was used to study the crystallite size of the prepared nanopowders. Perkin-Elmer LS-55- UV–Vis Spectrophotometer was used to study the absorption characteristics of the prepared samples. Photoluminescence spectra and the lifetime measurements were performed at room temperature using the Hitachi F-7000 fluorescence spectrophotometer.

3 Results and discussion

3.1 XRD analysis

The XRD patterns of prepared powder samples are shown in Fig. 1. The patterns show a single cubic phase and they match with the standard patterns of cubic $MgAl_2O_4$ (ICSD file no 172280) with lattice parameter (a) = 8.086 Å [16]. Most intense peak (113) was used to calculate the average lattice parameter (a) and it was found to be 8.086 Å (see Table 1) which is similar to the previously reported value by Peterson et al. [16] and the ICSD file no 172280. The motive why there is no change in a as shown in Table 1 will further be explained in Fig. 2. The patterns clearly show that doping and varying AP do not change the cubic crystal structure of $MgAl_2O_4$. No impurities were traced from the XRD patterns, which confirms that prepared samples were pure and single phase.

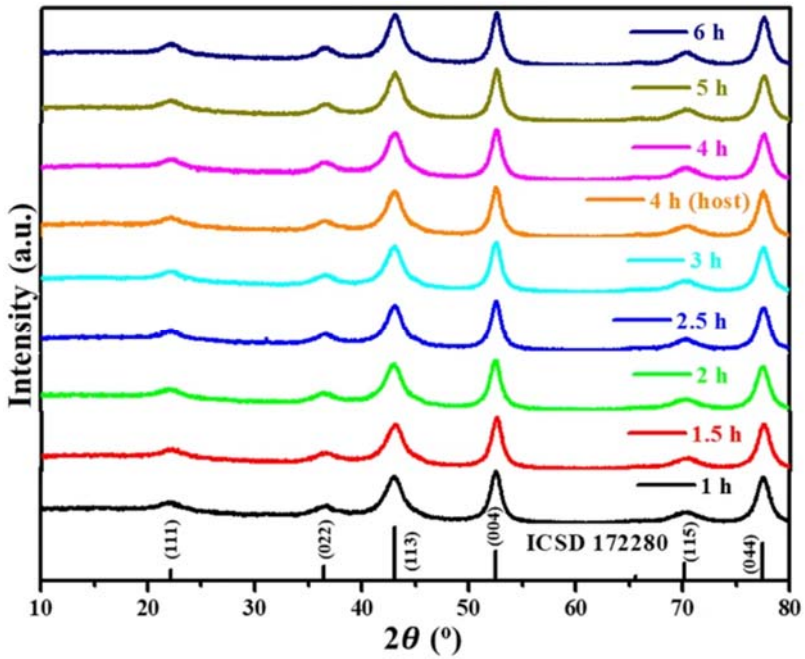

Fig. 1. The XRD pattern of the un-doped and $MgAl_2O_4$:0.1% Mn^{2+} at various APs

Table 1. Summary of the sample identification, 2θ, FWHM, d spacing, lattice parameters and crystallite size

AP (h)	2θ (degrees)	FWHM (rads)	d spacing (nm)	a (Å)	D (nm)
1	46.53	0.02048	0.2438	8.086	9
1.5	46.53	0.02025	0.2438	8.086	9
2	46.51	0.02104	0.2438	8.086	9
2.5	46.58	0.01975	0.2438	8.086	9
3	46.53	0.01982	0.2438	8.086	9
4	46.61	0.01966	0.2438	8.086	9
4*	46.58	0.01950	0.2438	8.086	9
5	46.55	0.01926	0.2438	8.086	9
6	46.55	0.01863	0.2438	8.086	10

*Un-doped sample

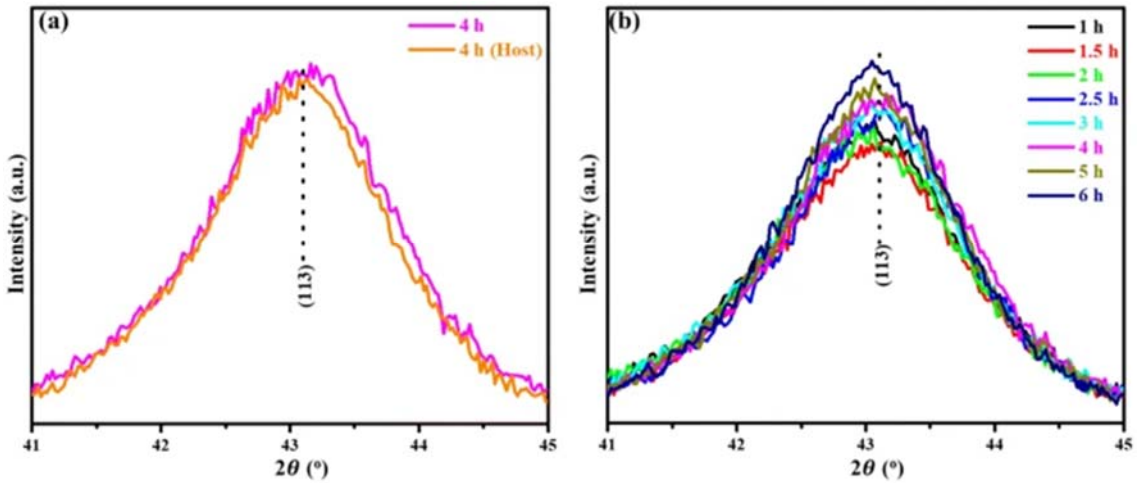

Fig. 2. The XRD analysis of the (113) diffraction peak of **a** host (AP = 4 h) and 4 h and **b** at various APs

The crystallite sizes were estimated and calculated from the (113) diffraction peak using the Scherrers's [17] equation:

$$D = \frac{0.9\lambda}{\beta(\cos\theta)} \tag{1}$$

where λ is the wavelength of the incident X-rays, θ is the diffraction angle and β is the full width of the diffraction line at half maximum intensity (FWHM), respectively. The estimated values are presented in Table 1. Generally, it can be noticed that the crystallite sizes of all prepared samples are similar. These results suggest that the AP did not significantly affect the crystallite sizes of the prepared samples even though there is a slight increase at 6 h compared to the other samples. The observed similar diffraction angles for all samples could be the fact that AP did not affect the crystal structure.

Figure 2 shows the analysis of the (113) diffraction peak. Figure 2a shows the un-doped and Mn^{2+} doped samples both at AP = 4 h, it is observed that there is no peak shift to higher or lower angle. Yuting et al. [18] reported on the study of the synergistic effect of N-decorated and Mn^{2+} doped ZnO nanofibers with enhanced photocatalytic activity. They have observed that by varying Mn^{2+} there was a shift to lower diffraction angle compared to un-doped ZnO.

The peak shift to lower angle was attributed to Mn^{2+} ions occupying the positions of the Zn^{2+} ions due to its larger ionic radius being lager than that of Zn^{2+}. On the other hand, Li et al. [12] observed a slight decrease in lattice parameter with the increase of Mn^{2+} content. This was attributed to the substitution of the smaller size of Mn^{2+} by larger sizes. However, in this study no peak shift is observed. This could be the small amount of Mn^{2+} content used. No peak shift is observed for powder samples at varying APs shown in Fig. 2b. There is a slight increase in diffraction intensity for the sample annealed at 1 h compared to 6 h. The observed slight increase in diffraction intensity and crystallite at 6 h may be dependent on AP [12, 19].

3.2 EDS analysis

The elemental composition of the un-doped sample at AP = 4 h shown in Fig. 3 was identified using the EDS technique. The spectra confirm the presence of Mg, Al and O as expected for the un-doped sample. Note that all the doped samples at various APs which are not shown in Fig. 3 did not show any presence of Mn and this may be attributed to the very low Mn^{2+} concentration used in this study. The observed additional peak of carbon (C) can be attributed to the sample mounting on the carbon tape during the sample preparation prior to the EDS measurements. No other impurities were detected by the EDS which agrees well with the XRD results shown in Fig. 1.

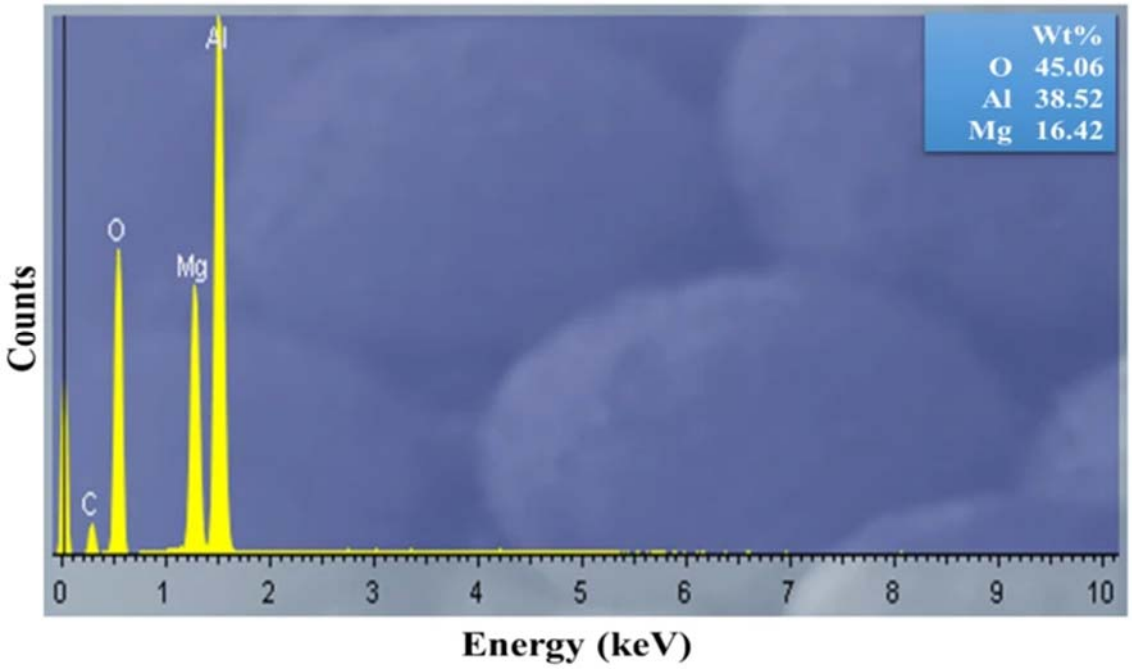

Fig. 3. The EDS spectrum of the un-doped sample

The EDS elemental map of the un-doped sample is shown in Fig. 4. The individual and layered elements show that Mg, Al and O are homogeneously distributed over the surface. No other impurities were detected by the elementary map. Thus, the results confirm the XRD results discussed in Fig. 1.

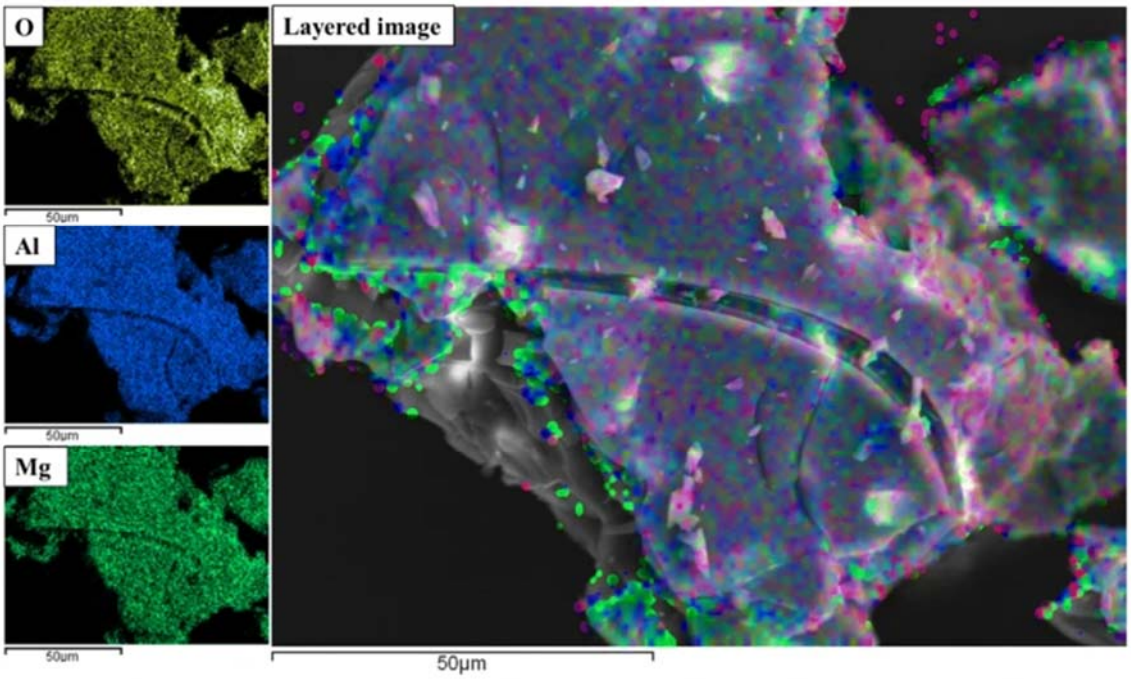

Fig. 4. The EDS elemental map of the un-doped $MgAl_2O_4$ at AP = 4 h

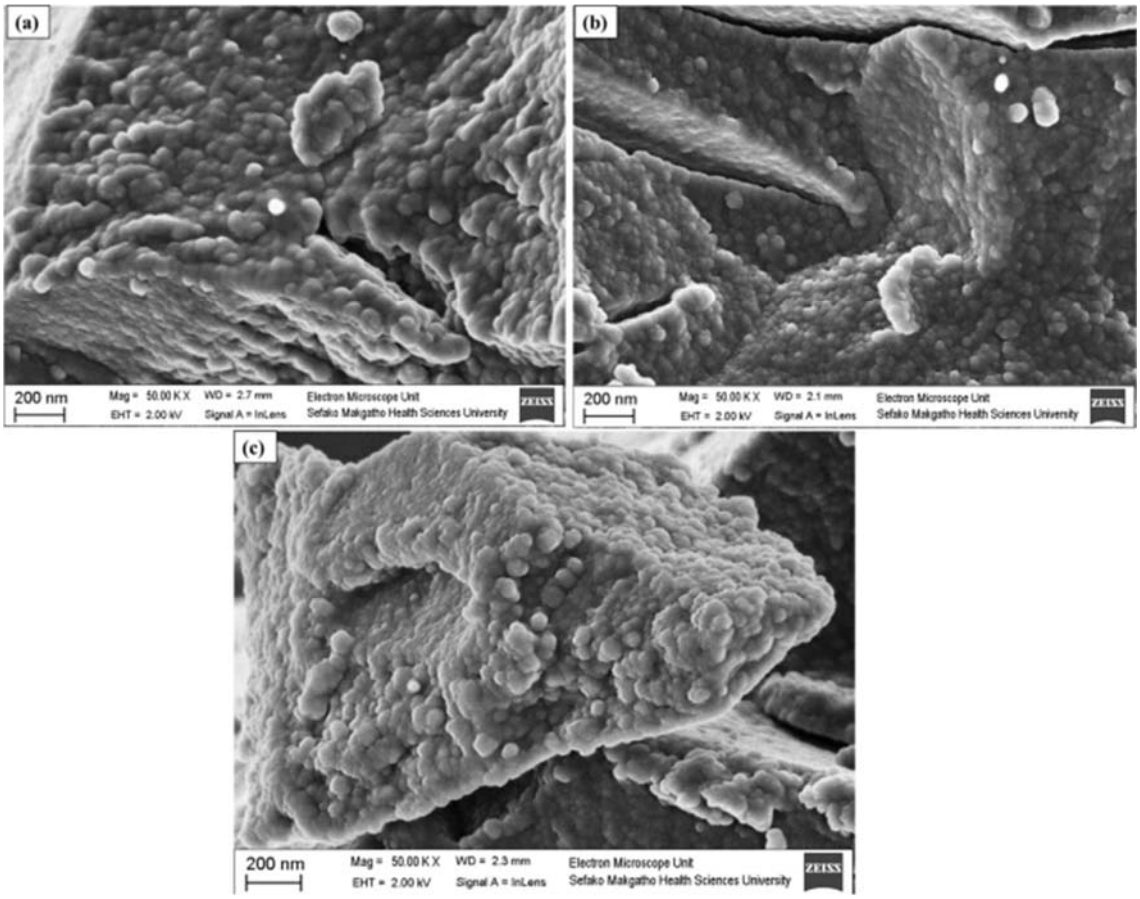

Fig. 5. SEM images of the $MgAl_2O_4$:0.1% Mn^{2+} samples at **a** AP = 4 h (host), **b** AP = 4 h and **c** AP = 6 h

3.3 SEM analysis

The prepared nanopowder samples of the un-doped and $MgAl_2O_4$:0.1% Mn^{2+} at various APs are shown in Fig. 5. Figure 5a shows the un-doped sample (AP = 4 h), which illustrates a rough surface with spherical and agglomerated particles. Figure 5b shows the 0.1% Mn^{2+} doped at AP = 4 h and in comparison to the un-doped sample in Fig. 5a, the results show that doping does not influence the surface morphology which agrees well with the XRD results. Figure 5c shows the AP = 6 h sample, which also resembles the same micrographs shown in Fig. 5a, b. When looking at Fig. 5b, c, it can be observed that there is a slight increase in particle size as AP was increased. The results agree with the estimated crystal size shown in Table 1. Hence, it can be concluded that doping and AP do not influence the shape. Varying AP slightly influences the particle sizes. The average measured particle sizes from SEM images in Fig. 5a–c were estimated to be 13, 14 and 17 nm, respectively. The average particle sizes are reasonable when compared to the values estimated by the XRD results in Table 1. The particle distribution from imagej is shown in Fig. 6a–c, respectively.

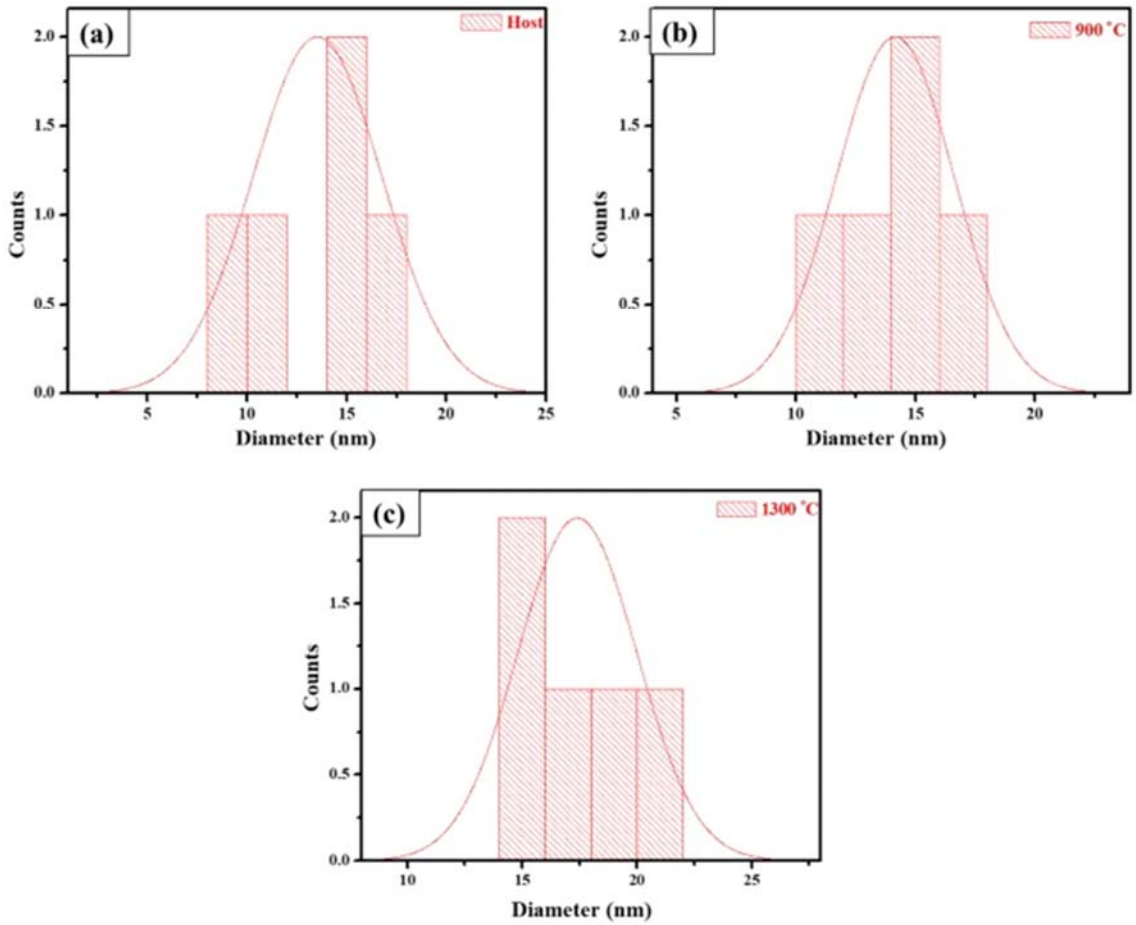

Fig. 6. Particle distribution of the $MgAl_2O_4$:0.1% Mn^{2+} samples at **a** AP = 4 h (host), **b** AP = 4 h and **c** AP = 6 h

3.4 TEM analysis

Figure 7 shows the TEM image of the Mn^{2+} doped at AP = 4 h to confirm the crystallitessize. The results show that the crystallites are agglomerated and the average crystallite size seems

to be below 15 nm, which agrees very well with the XRD and SEM results in Figs. 1 and 5, respectively.

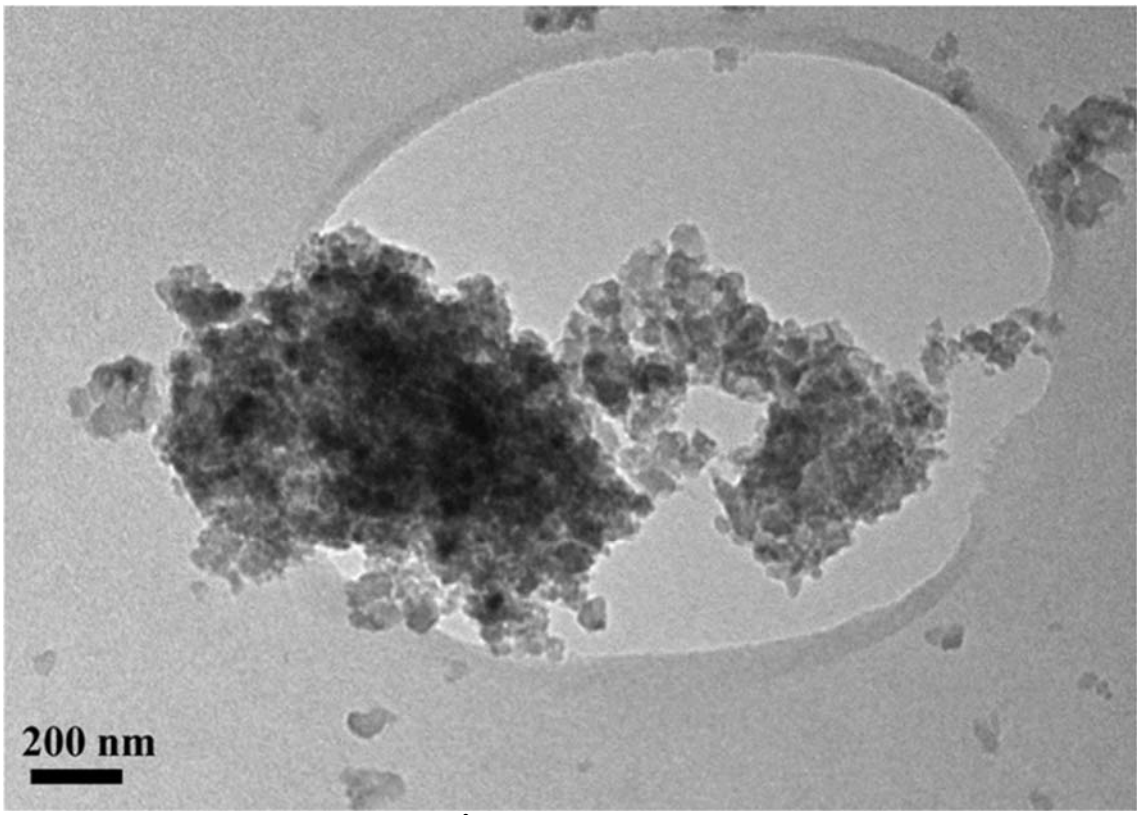

Fig. 7. TEM image of the $MgAl_2O_4$:0.1% Mn^{2+} at AP = 4 h

3.5 UV–Vis analysis

Figure 8a illustrates the reflectance absorption spectra of the un-doped and $MgAl_2O_4$:0.1% Mn^{2+} at various APs. The results revealed that there are several absorption peaks traced around 215, 255, 310 and 474 nm. The peak at 215 nm can be attributed to originate from the band-to-band of the un-doped material related to the reported absorption band at 223 nm [20]. Absorption band at 310 nm may be attributed to the change of lamp on the UV–Vis system [21]. The absorption bands at 255 can be attributed to arise from the $O^{2-} \rightarrow Al^{3+}$ charge transition due to the excitation of electrons from the valence band gap of O(2p) to conduction band of Al(3d) [22]. The band around 474 is associated with the energy levels of Mn^{2+} doping ($^4T_1 \rightarrow {}^6A_1$) substituting the Mg-sites. When looking at the results, mainly comparing the un-doped and 4 h doped sample it can be observed that doping does not affect the absorption edges of the un-doped material. We note that as the AP increases, the intensity of the absorption increases mainly comparing between 1 and 6 h samples, respectively. The results can be attributed to the increase in crystallinity by increasing AP [23].

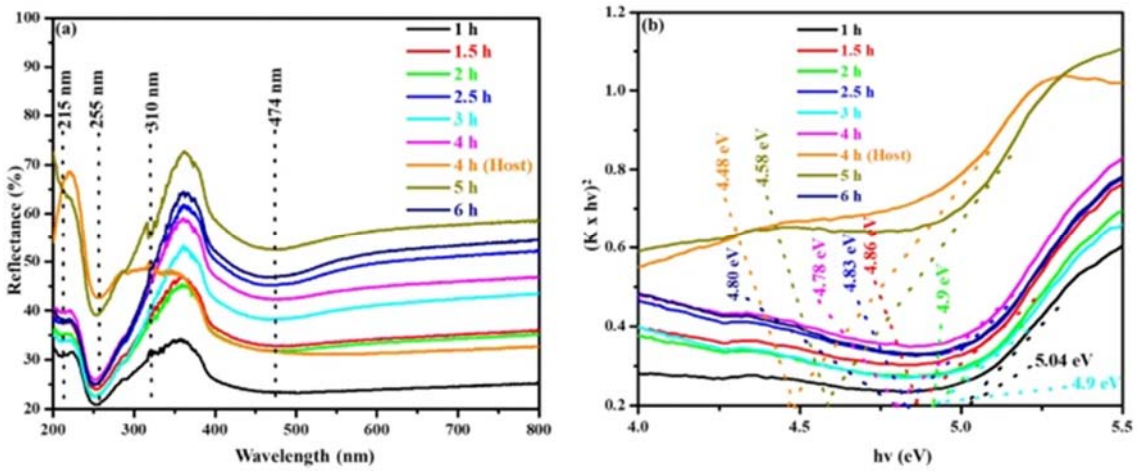

Fig. 8. a The diffuse reflectance spectra of the un-doped and $MgAl_2O_4$:0.1% Mn^{2+} at various APs and **b** Kubelka–Munk function of un-doped and $MgAl_2O_4$:0.1% Mn^{2+}

Figure 8b illustrates the Kubelka–Munk function $K = (1 - R)^2/2R$ [24]. The optical band gap energy values were estimated by extrapolation of the linear region of this plot to $(K \times hv)^2 = 0$. In this study n was chosen to be 2 because $MgAl_2O_4$ is a direct band gap material [25]. The energy band gap (E_g) for the estimated values is presented in Table 2 which is related to the reported value 5.23 eV [14]. The results show that doping slightly increased the E_g from 4.48 to 4.78 eV in comparison to the un-doped sample at 4 h. This behaviour is attributed to the Burstein-moss effect [26]. The results suggest that doping causes the conduction band to get occupied by the electron states which also pushes the Fermi level in the conduction band to higher energy level. As a result, this lead to an increase in the E_g. It can also be noted that the E_g slightly decreases with an increase in AP. The decrease in bad gap can be proposed to be due to the slight increase in crystallite size with an increase in AP as observed from the SEM and XRD results. We can then conclude that E_g can be tuned by the varying AP.

Table 2. Summary of the sample identification, optical band gap, decay times and CIE coordinates

Sample ID (h)	Band gap (eV)	Decay times (ms)		CIE (x;y)
		τ_1	τ_2	
1	5.04	2058.2 ± 1.6	3350.4 ± 255.5	(0.173;0.106)
1.5	4.86	2057.5 ± 1.4	3537.1 ± 262.1	(0.184;0.114)
2	4.90	2060.2 ± 1.7	3368.1 ± 219.6	(0.182;0.112)
2.5	4.83	2059.7 ± 1.6	3363.8 ± 229.7	(0.195;0.109)
3	4.91	2053.3 ± 1.3	3443.2 ± 289.1	(0.201;0.120)
4	4.78	2058.7 ± 1.4	3417.9 ± 223.1	(0.208;0.114)
4*	4.48	2081.4 ± 3.2	3222.4 ± 145.8	(0.160;0.019)
5	4.58	2057.2 ± 1.3	3556.5 ± 251.1	(0.256;0.141)
6	4.80	2055.9 ± 1.3	3545.9 ± 278.9	(0.238;0.133)

*Un-doped sample

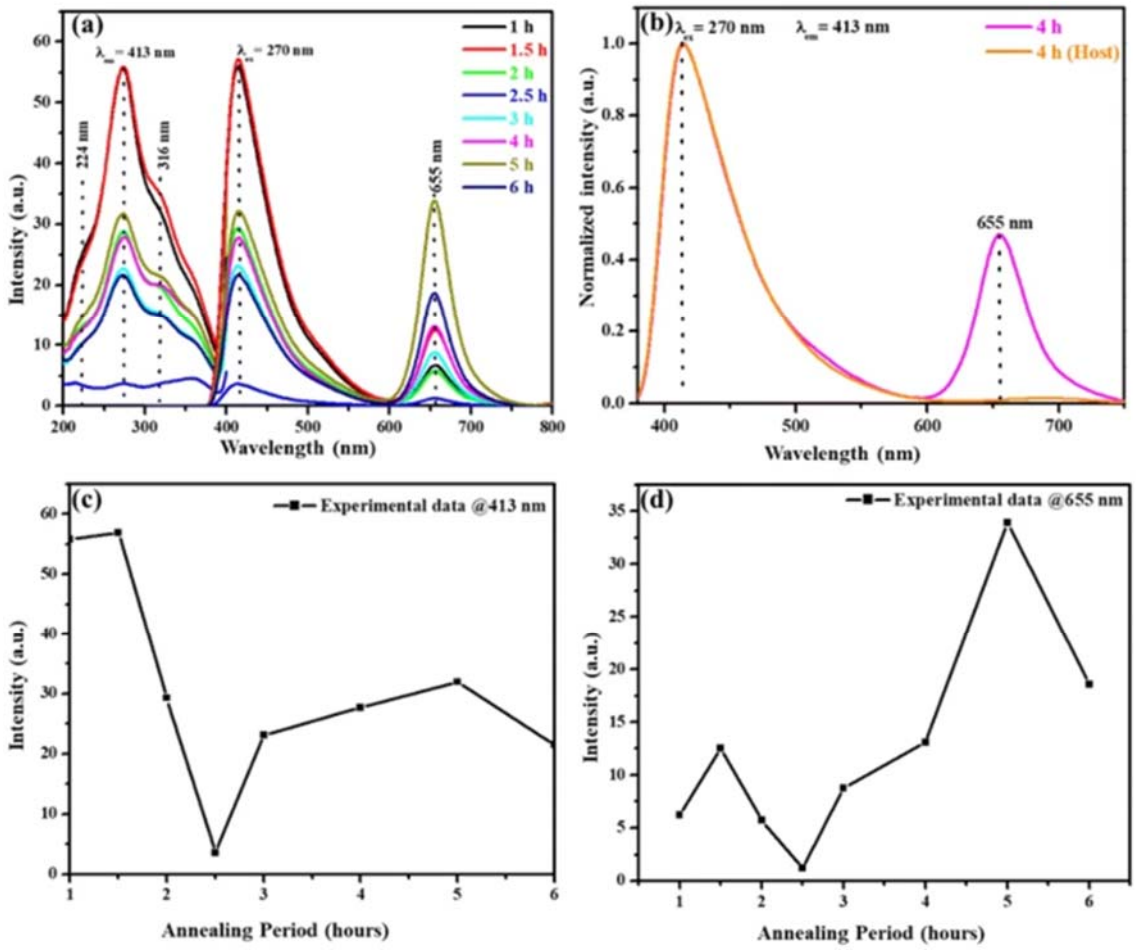

Fig. 9. a Emission and excitation spectra of un-doped and $MgAl_2O_4$:0.1% Mn^{2+} at various AP, **b** normalized emission spectra for the un-doped and doped $MgAl_2O_4$:0.1% Mn^{2+} at AP = 4 h and emission intensity as a function of AP **c** 423 nm and **d** 655 nm

3.6 PL analysis

The emission and excitation spectra of un-doped and $MgAl_2O_4$:0.1% Mn^{2+} at various APs are shown in Fig. 9a. PL spectra show that there are three excitation bands at around 224, 270 and 316 m when monitoring the emission at 413 nm. The 224 nm (5.54 eV) excitation peak is actually the band-to-band excitation [14]. The 270 nm may be attributed to the neutrally charged oxygen vacancy known as F center, on the other hand 316 nm is the positively charged oxygen vacancy known as F^+ center [27,28,29]. There are two emission peaks located at 413 and 655 nm as shown in Fig. 9a. The major peak at 413 nm (violet) is attributed to the defect level within the un-doped material [30]. The 655 nm (red) emission peak is attributed to the transition $^4T_1 \rightarrow {}^6A_1$ of Mn^{2+} ion [31]. The normalized emission intensity of un-doped and Mn^{2+} doped sample both at AP = 4 h is illustrated in Fig. 9b. It reveals the origin of each emission peak, that is the 413 and 655 nm originated from the same source as mentioned above. Figure 9c shows the emission intensity as a function of AP for 413 nm emission. The 1.5 h sample has the highest emission intensity and we notice a fluctuation in emission intensity as AP is increased. This could be caused by the defect level of doped samples during excitation. We observe similar behaviour for the 655 nm emission

intensity as a function of AP as shown in Fig. 9d. The 5 h sample has the highest intensity. The fluctuation could be due to the defect levels of Mn^{2+} ions during excitation.

The optimum excitation wavelength was obtained by exciting the un-doped sample at various excitation wavelengths as shown in Fig. 10a. Gaussian behaviour of the excitation wavelength as a function of emission intensity is shown in Fig. 10b. The results suggest that the optimum excitation wavelength for the un-doped sample is 270 nm, which serves as a reason why we excited all samples with 270 nm.

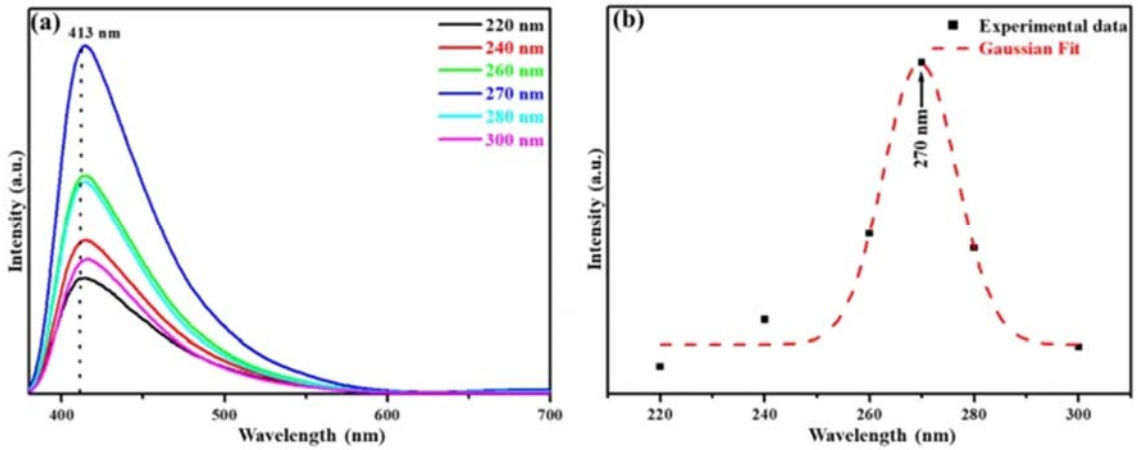

Fig. 10. a Emission spectra of the un-doped sample (AP = 4 h) at various excitation wavelengths and **b** the emission intensity as a function of excitation wavelength

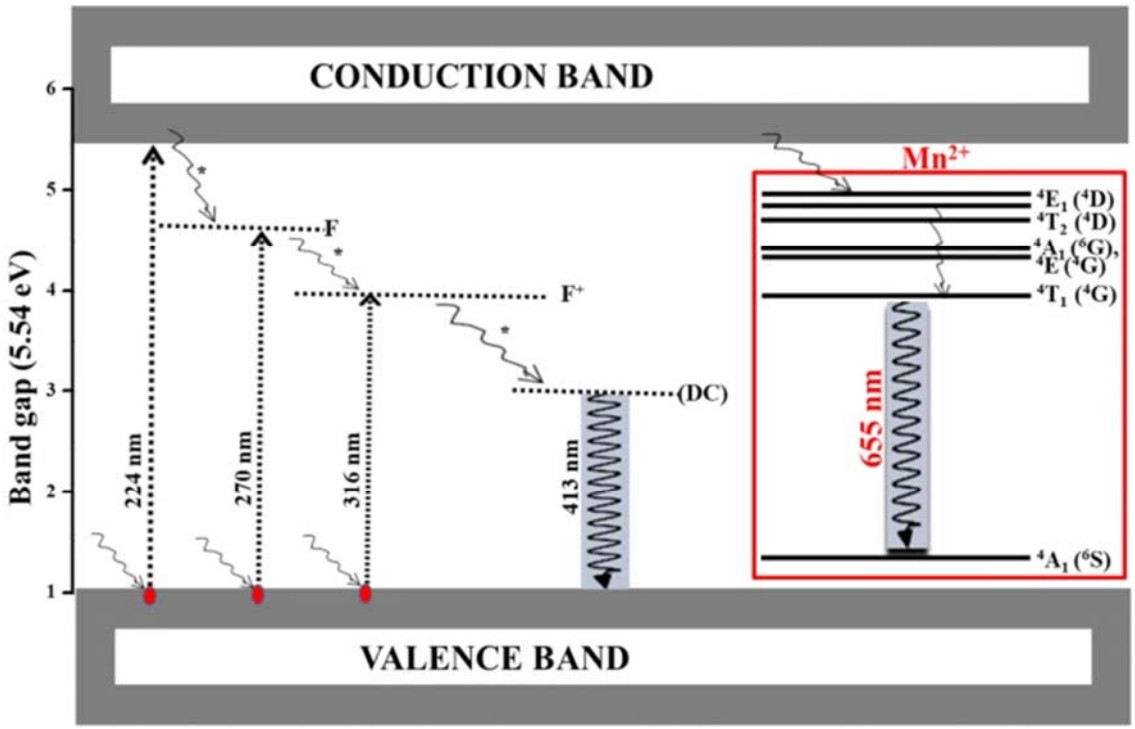

Fig. 11. Proposed excitation and emission pathway mechanisms of the un-doped and $MgAl_2O_4$:0.1% Mn^{2+}

Figure 11 shows the proposed pathway mechanism for the un-doped and $MgAl_2O_4$:0.1% Mn^{2+}. From the mechanism it can be clearly seen that the 224 nm excitation wavelength is a band to band and it is used to estimate the band gap energy (5.54 eV). The 270 and 316 nm show that there are defect levels within F and F^+ that can act as the trapping centers of excited electrons [14]. The mechanism also shows that there are two emission peaks located at 413 nm which are associated with the un-doped defect centres (DC) and 655 nm which originates from the transition $^4T_1 \rightarrow {}^4A_1$ of Mn^{2+} ion. The emissions occur in this way; the electrons that had absorbed enough energy get excited from the valence band (VB) to the conduction band (CB) [14]. They lose energy after the excitation and some electrons get trapped within the F and F^+ centers, resulting in the emission at 413 nm. The 655 nm emission from the Mn^{2+} ion also resulted from the excitation wavelength of 270 nm.

The PL life time decay of all the prepared nanopowder samples is shown in Fig. 12a. This phosphorescence life time decay was done at 413 nm emission and 270 nm excitation wavelengths. Results show that all the prepared nanopowder samples have the same phosphorescence mechanism irrespective of the AP. All the decay curves were better fitted using the second-order decay shown in Eq. (2) [30]

$$I(t) = I_o + A_1^{(-t/\tau 1)} + A_2^{(-t/\tau 2)} \quad (2)$$

where I represents the phosphorescent intensity, I_0 is the initial luminescence intensity, A_1 and A_2 are constants which contribute to the fast and slow decay components and t is the time of measurement. The τ_1 and τ_2 are the fast and slow decay time values which are shown in Table 2.

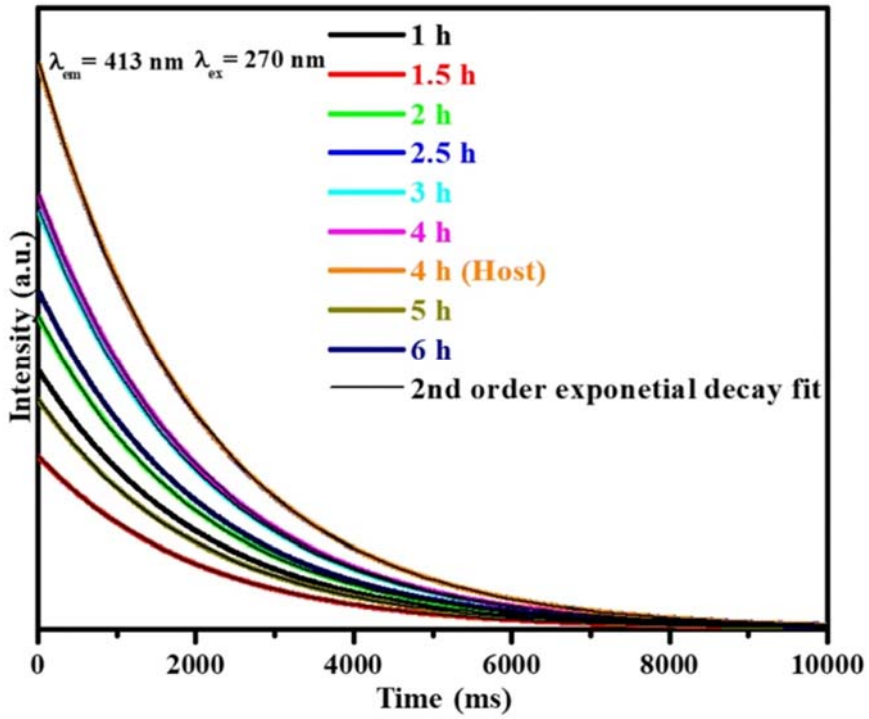

Fig. 12. The decay curve of the un-doped and $MgAl_2O_4$:0.1% Mn^{2+} at various APs

CIE colour diagram of the prepared powders at various APs determined using the CIE coordinate calculator software is shown in Fig. 13. The colour coordinates were estimated from the emission spectrum with excitation at 270 nm and are shown in Table 2. It can be clearly seen from the diagram that the colour shift from bluish to the violet when increasing the AP. It can be concluded that the emission colour can be turned by varying the AP.

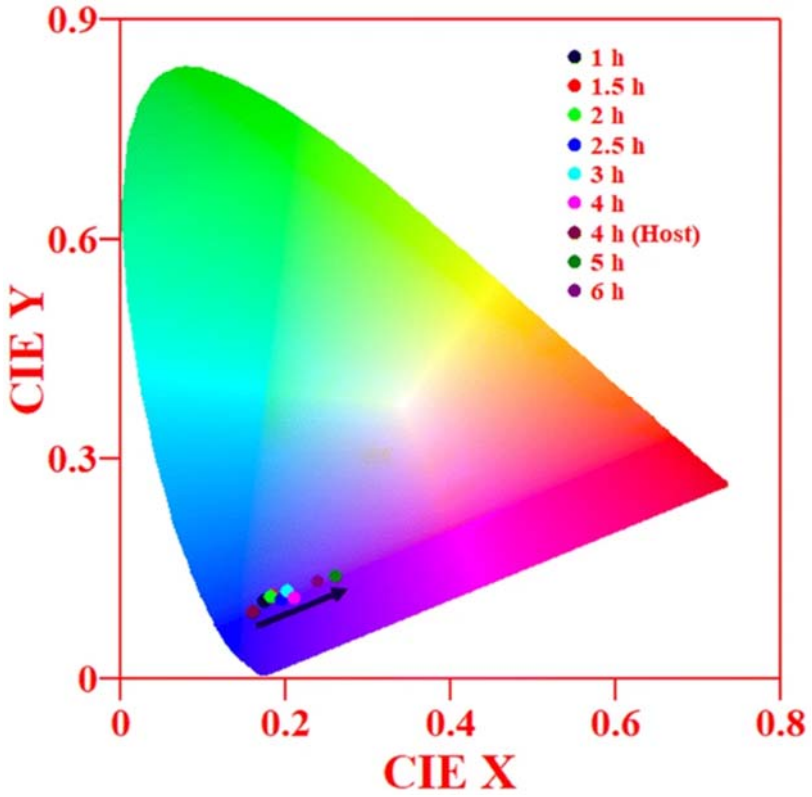

Fig. 13. CIE diagram of the un-doped and $MgAl_2O_4$:0.1% Mn^{2+} at various APs

4 Conclusion

The sol–gel method was successfully used to prepare the un-doped and $MgAl_2O_4$:0.1% Mn^{2+} nanopowders. XRD results showed that all samples consisted of a cubic structure. The crystallite sizes were slightly influenced by varying AP. SEM images showed that doping did not influence the morphology of the nanopowders and AP slightly increases the particle size. UV–Vis results showed that the E_g of the nanopowders can be tuned by varying AP. The PL results showed two emissions located at around 413 nm (blue) attributed to the defect levels within the un-doped material and 655 nm (red) was attributed to the $^4T_1 \rightarrow {}^6A_1$ transitions of Mn^{2+}. The emission colour was tuned by varying the AP shown by the CIE results. The prepared nanopowders can be a potential candidate for the solid-state light source such as LEDs.

Acknowledgements

This work is supported by the South African National Research Foundation (NRF) Thuthuka programme (Fund Numbers: UID 99266 and 113947), NRF incentive funding for rated researchers (IPRR) (Grant No: 114924). Dr James Wesley-Smith at Electron Microscopy

Unit at Sefako Makgatho Health Science University is acknowledged for the SEM and TEM imagings.

References

1. S. Oshio, K. Kitamura, T. Shigeta, J. Lumin. Dis. Phos. Elec. Soc **146**, 392–399 (1999)

2. L. Cornu, M. Dutttine, M. Gaudon, V. Jubera, J. Matter. Chem. C **2**, 9512–9552 (2014)

3. L.H. Ha, P.T. Lanh, N.N. Long, T.T. Loan, J. Phys: Conf. Ser. **187**, 1742–6596 (2009)

4. H. Muraki, Y. Fujitani, Appl. Catal. **47**, 75–84 (1989)

5. J. Sehested, A. Carlsson, T.V.W. Janssens, P.L. Hansen, A.K. Datye, J. Catal. **197**, 200–209 (2001)

6. T. Sharmal, B.S. Arora, Int. J. Res. Adv. Tech. **3**, 2321–9637 (2015)

7. Y. Fan, X.B. Lu, Y.W. Ni, H.J. Zhang, M.W. Zhu, Y. Li, C. Jiping, Appl. Catal. B Envriron. **101**, 606–612 (2011)

8. J. Xiaolin, Z. Haijun, Y. Yongjie, L. Zhanjie, Mater. Sci. Eng. A **379**, 112–118 (2004)

9. R.E. Carter, J. Am, Ceram. Soc. **3**, 116–120 (1961)

10. C.T. Wang, L.S. Lin, S.J. Yang, J. Am, Ceram. Soc. **75**, 1151–2916 (1992)

11. L. Cornu, M. Duttine, M. Gaudon, V. Jubera, J. Mater. Chem. C **1**, 1–3 (2015)

12. S. Li, S.Y. Zhao, T.N. Ye, X.W. Wu, K.X. Wang, X. Wei, J.S. Chen, J. Comput. Biol. Poly. **5**, 17–25 (2017)

13. M. Wan, K. He, H. Hong, Q. Wang, Q. Chen, Cond. Matter. **547**, 111–119 (2018)

14. L.T. Melato, T.E. Motaung, O.M. Ntwaeaborwa, S.V. Motloung, Opt. Mater. **66**, 319–326 (2017)

15. R. Zhong, J. Zhang, H. Wei, X. Qi, M. Li, X. Han, Chem. Phy. Lett. **508**, 207–209 (2011)

16. R.C. Peterson, G.A. Lager, R.L. Hitterman, Am. Miner. **76**, 1455–1458 (1991)

17. B.D. Cullity, S.R. Sock, *Elements of X-ray Diffraction*, vol. 3 (Pearson Education, Reading, 2001), pp. 402–404

18. W. Yuting, C. Jing, Y. Suye, J.A. Enric, S. Muhammad, W. Ziyuan, P. Wei, Scie. Rep. **6**, 32711–32718 (2016)

19. S.V. Motloung, P. Kumari, L.F. Koao, T.E. Motaumg, T.T. Hlatshayo, M.J. Mochane, Mater. Today Commun. **14**, 294–301 (2018)

20. S.V. Motloung, B.F. Dejene, R.E. Kroom, O.M. Ntwaeaborwa, H.C. Swart, T.E. Motaung, Opt. **131**, 705–712 (2017)

21. S.V. Motloung, K.G. Tshabalala, R.E. Kroon, T.E. Hlatshwayo, M. Mlambo, S. Mpelane, J. Mol. Struct. **1175**, 241–252 (2019)

22. Y. Mostafa, S.I. Nassar, S.A. Ahmed, Mol Bio Spectro **131**, 329–334 (2014)

23. S.V. Motloung, M. Tsega, F.B. Dejene, H.C. Swart, O.M. Ntwaeaborwa, L.F. Koao, T.E. Motaung, M.J. Hato, J. Alloy Comput. **677**, 72–79 (2016)

24. S.F. Wang, G.Z. Sun, L.M. Fang, L. Lei, X. Xiang, X.T. Zu, Sci. Rep. **5**, 12849–12854 (2015)

25. S.K. Sampath, D.G. Kanhere, R. Pandey, J. Phys, Condens. Matter **11**, 3635–3644 (1999)

26. B.E. Sernelius, K.F. Berggren, Z.C. Zin, I. Hamberg, C.G. Graqvist, Phys. Rev. B **37**, 8–10244 (1988)

27. S.S. Raj, S.K. Gupta, V. Grover, K.P. Muthe, V. Natarajan, A.K. Tyagi, J. Mol. Struct. **1089**, 81–85 (2015)

28. G.P. Summers, G.S. White, K.H. Lee, J.H. Crawford Jr., Phys. Rev. B **21**, 6–15 (1980)

29. A. Ibarra, D. Bravo, F.J. Lopez, F.A. Garner, J. Nucl. Mater. **336**, 156–162 (2005)

30. V.M. Maphiri, F.B. Dejene, S.V. Motloung, Res. Phys. **7**, 3510–3521 (2017)

31. R. Zhong, J. Zhang, H. Wei, X. Qi, M. Li, X. Han, Chem. Phys. Lett. **508**, 207–209 (2011)